www.lajss.org
Latin American Journal of Solids and Structures 4 (2007) 61–85

Spectral/HP finite elements applied to linear and non-linear structural elastic problems

Alberto Costa Nogueira Jr.[1] and Marco L. Bittencourt[2,*]

[1]Thorus Scisoft Tecnologia da Informação Ltda., Campinas, SP – Brazil
[2]Departamento de Projeto Mecânico, Faculdade de Engenharia Mecânica,
Universidade Estadual de Campinas, Campinas, SP – Brazil

Abstract

The main purpose of this paper is to demonstrate the applicability of the Spectral/*hp* Finite Element Method, originally developed to CFD problems [17], for the solution of linear and non-linear structural elastic problems using 3D non-structured meshes. Before achieving this goal, we present a previous study considering the selection of a set of hierarchical basis functions suitable to elliptic problems. This study compares some triangular hierarchical basis available in the literature in terms of the numerical conditioning resulting from the solution of the Poisson's problem with homogeneous Dirichlet boundary conditions. Based on these prior results and on the computational benefits of a tensor formulation when dealing with high-order numerical integration and differentiation, the Spectral/*hp* framework due to [17] was adopted to solve linear and non-linear structural elastic problems. Numerical examples are used to validate the application of the Spectral/*hp* FEM in the context of the structural mechanics.

Keywords: FEM, Spectral/HP finite elements, linear and non-linear elasticity.

1 Introduction

The quality of the approximation of Boundary Value Problems (BVP) obtained from the application of the Finite Element Method (FEM) depends on the size and shape of the elements, the properties of the approximation space and the regularity of the solution [14, 16]. From the computational point of view, the choice of the basis for the approximation space influences the stability and efficiency of the numerical procedures used to calculate the approximated solution. In general the finite element basis consist of piecewise polynomial functions defined on the elements of the partition which discretizes the problem domain.

Specifically, the *p*-version of the FEM has the following main features [17, 28]: high-order numerical integration; numerical differentiation; appropriate shape functions; geometric mapping for arbitrary domains; global C_0 inter-element continuity; degrees of freedom numbering; application of boundary conditions; and post-processing of results.

*Corresp. author email: mlb@fem.unicamp.br Received 15 September 2006; In revised form 4 October 2006

The p-shape functions are associated to the topological entities (vertex, edge, face and body) of the elements. In general, these functions are built from one-dimensional Legendre and Chebyshev polynomials [10, 28, 31]. Hierarchical or modal p-basis are characterized by the following properties [17]: vertex modes have one magnitude at one vertex and are zero at all other vertices; edges modes have magnitude along one edge and are zero at all other edges and vertices; face modes have magnitude along one face but are zero along all other faces, edges and vertices. Hierarchy means that high order expansion sets X_{p+1} contains the terms of the lower order expansion sets X_p, i.e., $X_p \subset X_{p+1}$. A nodal basis denotes a non-hierarchical expansion which is associated with a set of nodal points and generally based upon Lagrange polynomials.

Many p-shape functions have been presented in the literature. Peano [24, 25] considered families of hierarchical interpolation functions for straight-side triangular elements that can be applied to any polynomial order. Each new degrees of freedom for $p \geq 2$ represents the p-th derivative of the current approximation. The functions are mapped directly onto the elements using barycentric coordinates. Katz & Rossow [18,26] extended Peano′s work with the definition of a reference element and the use of pre-computed universal matrices and vectors to increase the computational performance. Zienkiewicz presented functions for hierarchical quadrilateral elements with good condition number of the local matrices, easy achievement of inter-element continuity and the use of error estimators [33].

The classical hierarchical functions for quadrilaterals and hexahedra introduced by Szabó & Babuška in [28] have excellent sparsity and conditioning properties due to the use of Legendre polynomials and their fully tensorial nature [12, 20]. However, the functions for triangles and tetrahedra do not have similar properties and show an exponential increase of the local condition number with the element order p [2, 9].

Carnevali [9] introduced hierarchical shape functions for triangles and tetrahedra with the property that the p-th edge, face and body functions are orthogonal in the Laplace operator sense to the same functions with orders not superior to $p-2$, $p-3$ and $p-4$, respectively. This fact resulted in local stiffness matrices with better condition numbers and sparsity compared to the functions defined in [28].

Sherwin & Karniadakis [27] presented hierarchical shape functions for triangles and tetrahedra based on collapsed cartesian coordinates, tensorial product, Jacobi orthogonal polynomials and exact numerical integration using tensor product of one-dimensional Gauss-Jacobi quadrature [17]. The collapsed coordinate systems for triangles and tetrahedra are obtained from the cartesian coordinate systems defined on quadrilaterals and hexahedra, respectively.

Webb & Abouchakra [32] used Jacobi polynomials to define shape functions for the [0,1] 2-simplex reference triangle. The quadrature rule defined in [11] is used. The extension of these functions to tetrahedra are presented in [1] and also use pre-computed universal matrices.

Nogueira & Bittencourt [15] showed the advantages of using Jacobi polynomials to improve the computational efficiency and the sparsity of the local and global matrices. It was also verified that the functions proposed in [9] have an exponential increasing of the condition number with the element order but still inferior to that verified in the functions presented in [28].

Adjerid [2] proposed new functions for triangles and tetrahedra with better sparsity and condition properties when compared to [9,28]. These functions are based on [28] and use the orthogonalization of face (2D case) and face and body (3D case) functions. The strategy presented is very similar to that one used in [21,22] to define pre-condititioners for domain decomposition methods in meshes of hexahedral elements.

A fully tensorial-based procedure to construct nodal and modal shape functions for triangles and tetrahedral in barycentric coordinates was presented in [6]. Due to the use of tensorial product, the modal functions have a natural global C^0 inter-element continuity. A unified approach to construct h- and p-shape functions for quadrilaterals, hexahedral, triangles and tetrahedral based on the tensorial product of one-dimensional bases is in [7]. The approach uses indices to denote the one-dimensional polynomials in each tensorization direction. The appropriate manipulation of the indices allows the construction of hierarchical or non-hierarchial and inter-element continuous or non-continuous bases. In addition, a new tensorial basis for triangles is defined aiming to improve the sparsity profiles of the local finite element matrices. The use of tensorial based construction has advantages as the manipulation of only one-dimensional polynomials and their derivatives, better computational performance and simplified implementation of parallel procedures and use of one-dimensional integration rules [6].

In addition to the mesh discretization (structured or non-structured) and the use of tensorial product functions for triangles and tetrahedra, the properties of conditioning and sparsity of the local matrices are essential in the p-version of the FEM [4, 9, 12, 15, 29]. The local properties are determined by the way the shape functions are defined and influence indirectly the correspondent properties of the global matrices [9, 12, 34]. The improved numerical efficiency of the structured expansions arise from their tensorial product based construction. Following [17] to be competitive the unstructured expansions must be as efficient as the structured ones mainly when applied to time-dependent problems.

The purpose of this paper is to apply the Spectral/*hp* FEM [17], originally developed to CFD, to linear and non-linear elasticity problems. The paper is organized as follows. First a brief review of the Spectral/*hp* FEM is presented. After that, the linear and non-linear elasticity formulations are discussed. The condition number of p-basis are studied based on results of their application to the Poisson's problem solved using iterative methods. Finally, results obtained from the application to Spectral/*hp* FEM to linear and non-linear elasticity problems are presented.

2 The spectral/*hp* finite element method

The Spectral/*hp* FEM uses collapsed coordinate systems to define the shape functions for triangles and tetrahedra. Figure 1 illustrates the procedure to obtain the triangle $T^2 = \{(\xi,\eta) \mid -1 \leq \xi,\eta;\xi+\eta \leq 0\}$ from the square $R^2 = \{(a,b) \mid -1 \leq a,b \leq 1\}$. This transformation allows the use of tensorial product to write the shape functions for triangles. Due to the rational nature

of the transformation $(a,b) \longmapsto (\xi,\eta)$ ($a = \frac{1+\xi}{1-\eta} - 1$), additional terms are included in the local expressions of the shape functions in the coordinates (a,b) to obtain polynomial basis in the local triangular and quadrangular domains. Figure 2 shows the analogous 3-steps transformation to obtain the local tetrahedron T^3 from the hexahedron R^3 [17, 27].

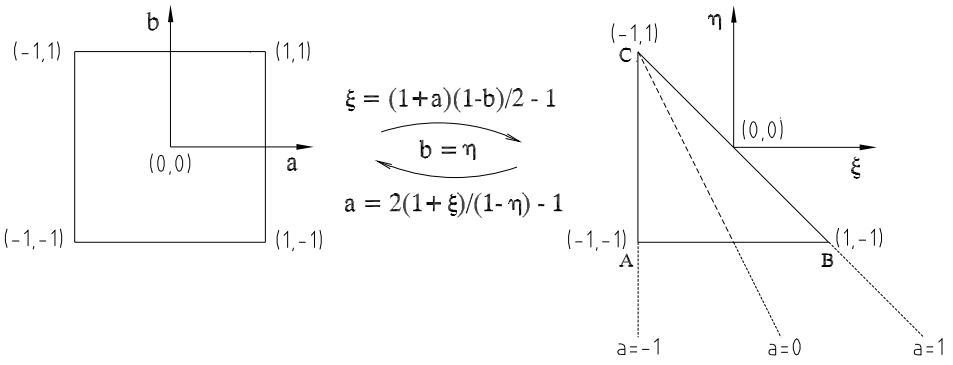

Figure 1: Mapping between quadrilateral and triangular domains [27].

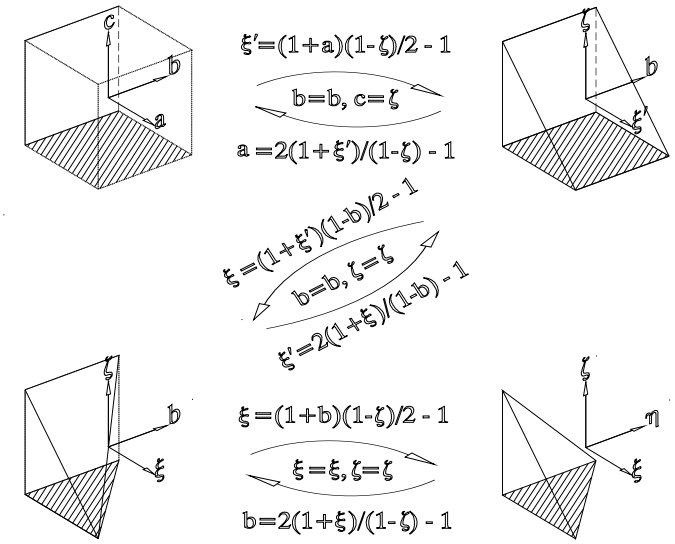

Figure 2: Mapping between hexahedron and tetrahedron domains [27].

Local and global operations are defined for the Spectral/*hp* FEM. The local operations are related to the numerical integration, numerical differentiation and the local-global mapping of the shape functions. Connectivity manipulation and degree of freedom numbering are the main global operations. Aspects of the numerical integration and differentiation are discussed here

briefly. Detailed analysis of the local and global operations, and the appropriate application of boundary conditions, are presented in [17].

The numerical integration in the tetrahedron domain $T^3 = \{(\xi,\eta,\zeta) \mid -1 \leq \xi,\eta,\zeta; \xi+\eta+\zeta \leq -1\}$ uses the collapsed transformation illustrated in Figure 2 which are expressed by the following relations

$$a = 2\frac{(1+\xi)}{(-\eta-\zeta)} - 1, \quad b = 2\frac{(1+\eta)}{(1-\zeta)} - 1, \quad c = \zeta, \tag{1}$$

For the linear and non-linear elasticity problems, the following general expression has to be integrated

$$\int_{T^3} u(\xi,\eta,\zeta)d\xi d\eta d\zeta = \int_{-1}^{1}\int_{-1}^{1}\int_{-1}^{1} u(a,b,c)Jdadbdc\,, \tag{2}$$

where the Jacobian J of the $R^3 \longrightarrow T^3$ transformation is given by

$$J = \frac{\partial(\xi,\eta,\zeta)}{\partial(a,b,c)} = \left(\frac{1-b}{2}\right)\left(\frac{1-c}{2}\right)^2. \tag{3}$$

The numerical integration of (2) from the tensorial product of one-dimensional quadrature rules is

$$\begin{aligned} &\int_{-1}^{1}\int_{-1}^{1}\int_{-1}^{1} u(a,b,c)\left(\frac{1-b}{2}\right)\left(\frac{1-c}{2}\right)^2 dadbdc \\ &= \sum_{i=0}^{Q_1-1} w_i \left\{ \sum_{j=0}^{Q_2-1} w_j \left\{ \sum_{k=0}^{Q_3-1} w_k u(a_i,b_j,c_k)\left(\frac{1-b_j}{2}\right)\left(\frac{1-c_k}{2}\right)^2 \right\} \right\}, \end{aligned} \tag{4}$$

where a_i, b_j and c_k are tensorial-based coordinates of the Q_1, Q_2 and Q_3 quadrature points in each spatial direction a, b and c, respectively; w_i, w_j and w_k are the respective weights of the Gauss quadrature.

The Gauss-Jacobi quadrature is defined by [17]

$$\int_{-1}^{1}(1-z)^\alpha(1+z)^\beta f(z)dz = \sum_{i=0}^{Q-1} w_i^{\alpha,\beta} f(z_i^{\alpha,\beta}), \tag{5}$$

where $w_i^{\alpha,\beta}$ and $z_i^{\alpha,\beta}$ are the weights and coordinates of the integration points for an appropriate selection of the weights α and β of the Jacobi polynomial. For $\alpha = \beta = 0$, the Gauss-Legendre quadrature is obtained. The boundary points of the domain may be included in the numerical integration when using the Gauss-Jacobi quadrature with Lobatto and Radau distributions of points [17].

Based on the previous definition, the number of integration points for the consistent integration of (4) may be reduced with the inclusion of the Jacobian terms in the weights. For that

purpose, ($\alpha = 0$, $\beta = 0$), ($\alpha = 1$, $\beta = 0$) and ($\alpha = 2$, $\beta = 0$) are selected, respectively, in the directions a, b and c. The integration on T^3 given in (4) may be written as

$$\begin{aligned} &\int_{-1}^{1}\int_{-1}^{1}\int_{-1}^{1} u(a,b,c)\left(\frac{1-b}{2}\right)\left(\frac{1-c}{2}\right)^2 dadbdc \\ &= \sum_{i=0}^{Q_1-1} w_i^{0,0}\left\{\sum_{j=0}^{Q_2-1}\hat{w}_j^{1,0}\left\{\sum_{k=0}^{Q_3-1}\hat{w}_k^{2,0}u(a_i^{0,0},b_j^{1,0},c_k^{2,0})\right\}\right\}, \end{aligned} \tag{6}$$

where

$$\hat{w}_j^{1,0} = \frac{w_j^{1,0}}{2} \text{ and } \hat{w}_k^{2,0} = \frac{w_k^{2,0}}{4}. \tag{7}$$

The Gauss-Radau distribution is used in the η, ζ directions while the Gauss-Lobatto points are considered for the ξ direction as illustrated in Figure 3. This selection avoids multiple points on the vertices ($\xi = -1$, $\eta = -1$, $\zeta = 1$) and ($\xi = -1$, $\eta = 1$, $\zeta = 1$) and along the edge that connects these vertices. Therefore, the calculation on the singular points of the collapsed transformation is avoided. Although numerical perturbations would be expected when using singular integration points, [17] gave a theoretical proof demonstrating the boundness of the collapsed transformation over the singular points.

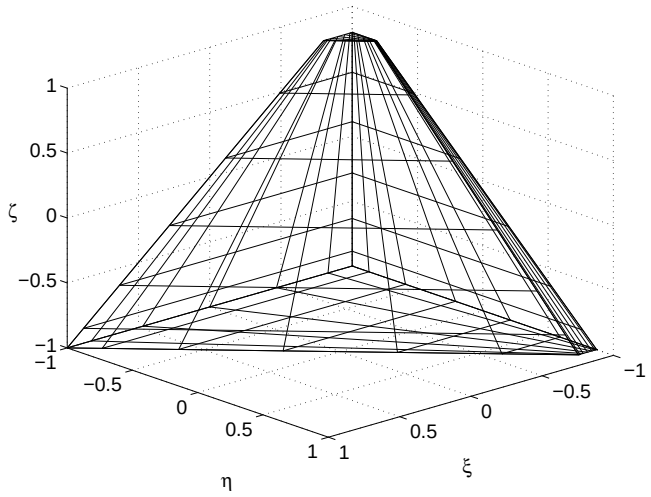

Figure 3: Quadrature points for the local tetrahedron T^3 with $Q_1 = Q_2 = Q_3 = 7$ and Gauss-Lobatto points in the ξ-direction and Gauss-Radau points in the η and ζ-directions [17].

The differential operators of the linear and non-linear elasticity problems are applied to the shape functions of the approximation space and evaluated on the integration points for each finite element of the mesh. The collocation differentiation may be used to calculate the derivatives of the shape functions on the integration points [17]. It is based on the representation of arbitrary

polynomial functions by Lagrange polynomials defined on the quadrature coordinates. The representation is a simple change of basis for the same polynomial space. Based on that, the local polynomial approximation for a one-dimensional function $u(\xi)$ is written as

$$u(\xi) = \sum_{p=0}^{P_1} \hat{u}_p \phi_p(\xi) = \sum_{p=0}^{P_1} u_p h_p(\xi) \tag{8}$$

where $\phi_p(\xi)$ are the interpolation functions of order $\leq P_1$, $h_p(\xi)$ are the Lagrange polynomials defined on the $P_1 + 1$ integration points and $\hat{u}_p$ and u_p are the coefficients of the approximation in the original and transformed basis, respectively.

Due to the collocation property of the Lagrange polynomials (i.e., $h_i(\xi_j) = \delta_{ij}$), the coefficients u_p are the values of the approximated function on the integration points, i.e.,

$$u_p = u(\xi_p). \tag{9}$$

Therefore, it is possible to express the derivative of the approximated function as

$$\frac{\partial u}{\partial \xi}(\xi) = \sum_{p=0}^{P_1} u_p \frac{\partial h_p}{\partial \xi}(\xi) = \sum_{p=0}^{P_1} u(\xi_p) \frac{\partial h_p}{\partial \xi}(\xi). \tag{10}$$

For the reference element T^3, which is mapped from the hexahedron R^3, the polynomial expansion of the function $u(a, b, c)$ in terms of Lagrange polynomials in the tensorial coordinates a, b and c is

$$u(a, b, c) = \sum_{p,q,r=0}^{P_1,P_2,P_3} \hat{u}_{pqr} \psi_{pqr}(a, b, c) = \sum_{p=0}^{P_1} \sum_{q=0}^{P_2} \sum_{r=0}^{P_3} u_{pqr} h_p(a) h_q(b) h_r(c), \tag{11}$$

where $\psi_{pqr}(a, b, c) = \phi_{pqr}(\xi, \eta, \zeta)$ are the basis functions represented in the tensorized space (a, b, c) and h_j (for $j = p, q, r$) are the Lagrange polynomials of order P_i $(i = 1, 2, 3)$.

Analogously to equation (10), the partial derivatives of the approximated function are

$$\frac{\partial u}{\partial a}(a, b, c) = \sum_{p=0}^{P_1} \sum_{q=0}^{P_2} \sum_{r=0}^{P_3} u_{pqr} \frac{\partial h_p(a)}{\partial a} h_q(b) h_r(c), \tag{12}$$

$$\frac{\partial u}{\partial b}(a, b, c) = \sum_{p=0}^{P_1} \sum_{q=0}^{P_2} \sum_{r=0}^{P_3} u_{pqr} h_p(a) \frac{\partial h_q(b)}{\partial b} h_r(c), \tag{13}$$

$$\frac{\partial u}{\partial c}(a, b, c) = \sum_{p=0}^{P_1} \sum_{q=0}^{P_2} \sum_{r=0}^{P_3} u_{pqr} h_p(a) h_q(b) \frac{\partial h_r(c)}{\partial c}. \tag{14}$$

The evaluation of the previous expressions on the integration points using the collocation property of the Lagrange polynomials gives

$$\frac{\partial u}{\partial a}(a_i,b_j,c_k) = \sum_{p=0}^{P_1} u_{pjk} \left.\frac{\partial h_p(a)}{\partial a}\right|_{a_i}, \tag{15}$$

$$\frac{\partial u}{\partial b}(a_i,b_j,c_k) = \sum_{q=0}^{P_2} u_{iqk} \left.\frac{\partial h_q(b)}{\partial b}\right|_{b_j}, \tag{16}$$

$$\frac{\partial u}{\partial c}(a_i,b_j,c_k) = \sum_{r=0}^{P_3} u_{ijr} \left.\frac{\partial h_r(c)}{\partial c}\right|_{c_k}. \tag{17}$$

The procedures for the collocation differentiation, which result from the evaluation of the derivatives of Lagrange polynomials, used in the previous expressions are discussed in [17] and are based on the distribution of points for the Gauss-Jacobi, Gauss-Legendre, Gauss-Radau and Gauss-Lobatto quadratures.

From expressions (15) to (17), the chain rule is applied to obtain the local partial derivatives with respect to the cartesian coordinates (ξ,η,ζ) of the reference element T^3, i.e.,

$$\nabla = \begin{pmatrix} \dfrac{\partial}{\partial\xi} \\ \dfrac{\partial}{\partial\eta} \\ \dfrac{\partial}{\partial\zeta} \end{pmatrix} = \begin{pmatrix} \dfrac{4}{(1-b)(1-c)}\dfrac{\partial}{\partial a} \\ \dfrac{2(1+a)}{(1-b)(1-c)}\dfrac{\partial}{\partial a} + \dfrac{2}{(1-c)}\dfrac{\partial}{\partial b} \\ \dfrac{2(1+a)}{(1-b)(1-c)}\dfrac{\partial}{\partial a} + \dfrac{(1+b)}{(1-c)}\dfrac{\partial}{\partial b} + \dfrac{\partial}{\partial c} \end{pmatrix}. \tag{18}$$

For the cases $b=1$ or $c=1$, the operator ∇ becomes singular. This problem may be avoided using Gauss-Radau quadrature along the b and c-directions.

3 Formulation of the linear and non-linear elasticity problems

The linear elasticity BVP is given by the following equations [28]

$$\begin{aligned} \mathrm{div}\sigma + \mathbf{b} &= \mathbf{0} \quad \text{em} \quad \Omega, \\ \mathbf{u} &= \bar{\mathbf{u}} \quad \text{em} \quad \partial\Omega^D, \\ \sigma\mathbf{n} &= \bar{\mathbf{t}} \quad \text{em} \quad \partial\Omega^N. \end{aligned} \tag{19}$$

where σ is the Cauchy tensorial field; $\mathbf{b}$ is the body load vector field defined on the Ω domain; $\mathbf{u}$ is the displacement vector field with prescribed values $\bar{\mathbf{u}}$ on the Dirichlet boundary $\partial\Omega^D$; $\mathbf{t}$ is the surface load vector field with prescribed values $\bar{\mathbf{t}}$ applied on the Neumann boundary $\partial\Omega^N$; and $\mathbf{n}$ is the normal vector field on $\partial\Omega^N$. For all examples presented in this paper, $\bar{\mathbf{u}} = \mathbf{0}$.

The material constitutive equation is given by the Hooke's law, i.e.,

$$\sigma(\mathbf{u}) = \mathsf{C} : \epsilon, \tag{20}$$

$$\epsilon(\mathbf{u}) = \frac{1}{2}\left(\nabla\mathbf{u} + \nabla\mathbf{u}^T\right). \tag{21}$$

where C is the elasticity tensorial field and ϵ is the infinitesimal strain tensorial field defined on the material points of the domain Ω.

The weak or variational form of the BVP (20) is expressed by:

Find the displacement vector field $\mathbf{u} \in \mathbf{V} = \{\mathbf{v}(\mathbf{x}) \in [H^1(\Omega)]^3 : \mathbf{v} = \mathbf{0}$ *on* $\partial\Omega^D\}$ *such as*

$$\int_\Omega \sigma(\mathbf{u}) : \epsilon(\mathbf{v})dV = \int_\Omega \mathbf{b}\cdot\mathbf{v}dV + \int_{\partial\Omega^N} \overline{\mathbf{t}}\cdot\mathbf{v}dS, \quad \forall\mathbf{v} \in \mathbf{V}, \tag{22}$$

where $H^1(\Omega)$ is the Sobolev space commonly used in the variational formulation of second-order problems.

The previous weak form may be expressed as

$$\mathcal{B}(\mathbf{u},\mathbf{v}) = \mathcal{F}(\mathbf{v}), \quad \forall\mathbf{v} \in \mathbf{V}, \tag{23}$$

where $\mathcal{B}(\mathbf{u},\mathbf{v})$ and $\mathcal{F}(\mathbf{v})$ are the bilinear and linear forms given by

$$\mathcal{B}(\mathbf{u},\mathbf{v}) = \int_\Omega \sigma(\mathbf{u}) : \epsilon(\mathbf{v})dV, \tag{24}$$

$$\mathcal{F}(\mathbf{v}) = \int_\Omega \mathbf{b}\cdot\mathbf{v}dV + \int_{\partial\Omega^N} \overline{\mathbf{t}}\cdot\mathbf{v}dS, \quad \forall\mathbf{v} \in \mathbf{V}. \tag{25}$$

Considering the finite dimensional subspace $\mathbf{S^p} \subset \mathbf{V}$, the p-version finite element approximation of (22) is expressed as [28]

$$\{\mathbf{u}\} = \sum_{i=1}^{n_p} [\mathbf{\Phi}_i]\{\hat{\mathbf{u}}_i\}, \tag{26}$$

where

$$[\mathbf{\Phi}_i] = \begin{bmatrix} \phi_x^i & 0 & 0 \\ 0 & \phi_y^i & 0 \\ 0 & 0 & \phi_z^i \end{bmatrix} \tag{27}$$

is the matrix of the global basis functions obtained here from the assembling of the local basis proposed for the Spectral/*hp* FEM; $\{\hat{u}_i\} = \{\hat{u}_x^i, \hat{u}_y^i, \hat{u}_z^i\}$ is the vector of the unknown degrees of freedom; and n_p is the dimension of the space $\mathbf{S^p}$. In [28], the space $\mathbf{S^p}$ is written formally as $\mathbf{S^p}(\Omega, \Delta, \mathbf{Q})$, where the parameters $\Omega, \Delta, \mathbf{Q}$ are the problem domain, the discretization mesh and the local-global mapping, respectively. The index $\mathbf{p}$ in $\mathbf{S}$ indicates the polynomial order of elements of the mesh.

Using the Galerkin approach, the substitution of (26) in (22) results in the approximated equation

$$\mathcal{B}_p(\{\mathbf{u}\},\{\mathbf{v}\}) = \mathcal{F}_p(\{\mathbf{v}\}), \quad \forall\{v\} \in \mathbf{V}, \tag{28}$$

where the discretized bilinear and linear forms are

$$\mathcal{B}_p(\{\mathbf{u}\},\{\mathbf{v}\}) = \int_\Omega ([D]\{\mathbf{v}\})^T [C]([D]\{\mathbf{u}\}) dV, \tag{29}$$

$$\mathcal{F}_p(\{\mathbf{v}\}) = \int_\Omega (b_x v_x + b_y v_y + b_z v_z) dV + \int_{\partial\Omega^N} (\bar{t}_x v_x + \bar{t}_y v_y + \bar{t}_z v_z) dS. \tag{30}$$

In the previous expression, $[C]$ is the isotropic elasticity matrix and its coefficients are expressed in terms of the material properties and $[D]$ is the following differential operator

$$[D] = \begin{bmatrix} \frac{\partial}{\partial x} & 0 & 0 \\ 0 & \frac{\partial}{\partial y} & 0 \\ 0 & 0 & \frac{\partial}{\partial z} \\ \frac{\partial}{\partial y} & \frac{\partial}{\partial x} & 0 \\ 0 & \frac{\partial}{\partial z} & \frac{\partial}{\partial y} \\ \frac{\partial}{\partial z} & 0 & \frac{\partial}{\partial x} \end{bmatrix}. \tag{31}$$

Equation (28) may be written as the following system of algebraic equations

$$[\mathbf{K}]\{\mathbf{u}\} = \{\mathbf{f}\}, \tag{32}$$

where $[\mathbf{K}]$ and $\{\mathbf{f}\}$ are the global stiffness matrix and equivalent load vector, respectively.

The material description is used here to formulate the non-linear elasticity problem of large deformation. The strain measure is given by the Lagrangian tensor, i.e., [8, 19]

$$\mathbf{E}(\mathbf{u}) = \frac{1}{2}\left(\nabla\mathbf{u} + \nabla\mathbf{u}^T\right) + \frac{1}{2}\nabla\mathbf{u}^T\nabla\mathbf{u}. \tag{33}$$

The equilibrium equation is given by [8, 19]

$$\mathrm{Div}\mathbf{S} + \bar{\mathbf{b}} = \mathbf{0}, \tag{34}$$

where $\mathbf{S}$ is the second Piolla-Kirchhoff stress tensor and $\bar{\mathbf{b}}$ is the material representation of the body load vector. The Hooke's law is used as the constitutive equation for the non-linear elasticity problem.

The related weak or variational form of the non-linear elasticity problem is:

Find the displacement vector field $\mathbf{u} \in \mathbf{V} = \{\mathbf{v}(\mathbf{x}) \in [H^1(\Omega)]^3 : \mathbf{v} = \mathbf{0}$ *on* $\partial\Omega^D\}$ *such that*

$$\int_\Omega \mathbf{S} : \delta\mathbf{E} dV = \int_\Omega \mathbf{b}\cdot\delta\mathbf{v} dV + \int_{\partial\Omega^N} \bar{\mathbf{t}}\cdot\delta\mathbf{v} dS, \tag{35}$$

where $\delta\mathbf{E} = D\mathbf{E}(\mathbf{v})[\delta\mathbf{v}]$ is the Gateaux differential of $\mathbf{E}$ in the direction $\delta\mathbf{v}$.

The finite element approximation of the previous weak form using the p-version is obtained from (26) and (27) and the following system of algebraic equations results

$$[\mathbf{K}(\mathbf{u})]\{\mathbf{u}\} = \{\mathbf{f}\}, \tag{36}$$

where $\mathbf{K}(\mathbf{u})$ is the non-linear global stiffness matrix. The Newton-Raphson procedure is used to linearize and solve the previous system of equations.

4 Results

This section presents results of the application of the Spectral/hp FEM to solve linear and non-linear elasticity problems using meshes of triangles and tetrahedra. Initially, a comparison of sets of p-shape functions presented in the literature is considered when applied to the Poisson's equation in two-dimensional domains. This previous analysis has been used to select the most appropriate set of p-basis functions to be applied in the solution of the elasticity problems presented in the following.

4.1 Comparison of p-shape functions

In [15] a comparison of the condition numbering and sparsity of the local mass and stiffness matrices of triangles and tetrahedra obtained from the application of p-basis presented in the literature were considered [1, 9, 27, 28, 32] and a new basis was proposed. This section presents the solution of algebraic global systems, obtained from the application of the mentioned p-basis to the Poisson's problem, by the standard and Jacobi pre-conditioning conjugate gradient methods [3].

The square and L-shaped domains illustrated in Figure 4 are considered. The load terms were chosen to result high gradients in the solution for the square domain and a smooth solution of the L-shaped domain as in this case there is a geometric singularity [23]. The respective analytical solutions for the square and L-shaped domains are

$$u(x,y) = xy(1-x)(1-y)\tan^{-1}\left[60\left(\frac{x+y}{\sqrt{2}} - 0.8\right)\right]. \tag{37}$$

and

$$u(x,y) = \frac{3}{2}r^{2/3}\sin\frac{2\theta}{3}(1-x^2)(1-y^2), \tag{38}$$

where $r = \sqrt{x^2+y^2}$ and $\theta = \tan^{-1}\left(-\frac{x}{y}\right)$. These solutions are plotted in Figures 4(c) and 4(f), respectively.

Figure 5 shows the number of iterations of the standard and Jacobi conjugate gradient methods using the convergence criterion $||[\mathbf{K}]\{\mathbf{u}\} - \{\mathbf{f}\}||_2/||\{\mathbf{f}\}||_2 \leq \epsilon$ for $\varepsilon = 10^{-6}$ versus

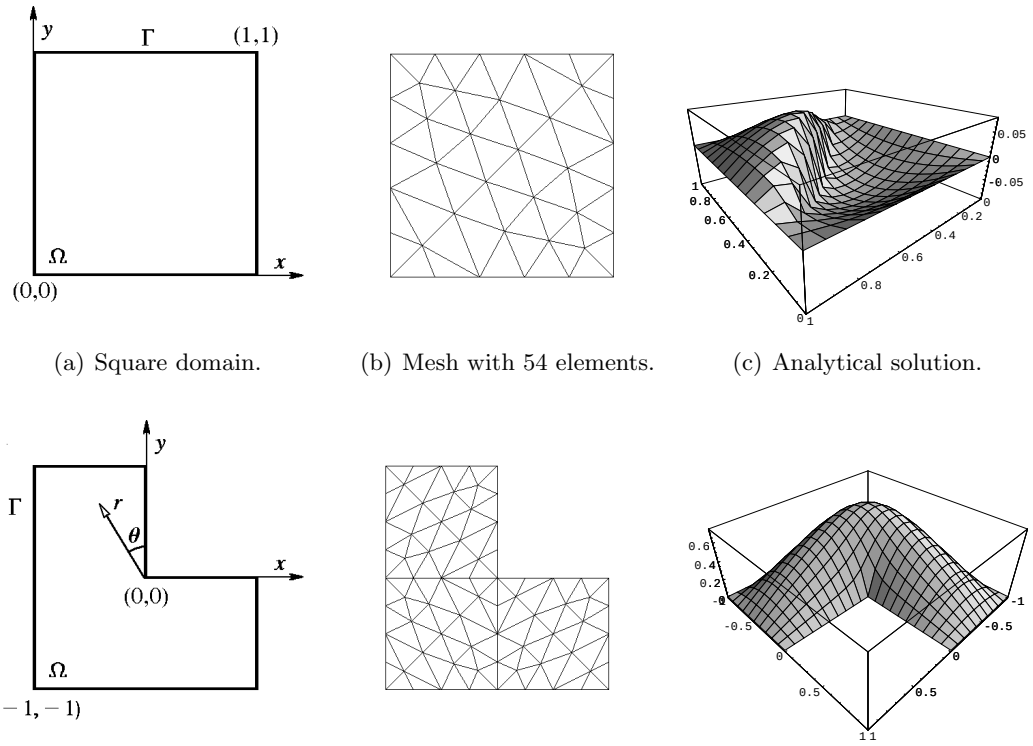

(a) Square domain. (b) Mesh with 54 elements. (c) Analytical solution.

(d) L-shaped domain. (e) Mesh with 108 elements. (f) Analytical solution.

Figure 4: Square and L-shaped domains, finite element meshes and analytical solutions [23].

the polynomial order $p = 2, 3, \ldots, 8$. The behaviour of the results are very close to those ones obtained for the local condition number of the stiffness matrices presented in [15]. The results also asserts the validity of the estimation of the global condition number in terms of the local behaviour presented in [34]. In addition, the theoretical relation between the number of iterations ($NIT(\varepsilon)$) of the conjugate gradient method and the condition number of the global stiffness matrices ($\kappa(A_{glob})$), i.e., [3]

$$NIT(\varepsilon) \leq \frac{1}{2}\sqrt{\kappa(A_{glob})}\ln(2/\varepsilon) + 1, \tag{39}$$

is also observed. Based on that, it is verified that the local analysis of the shape functions gives consistent information about the behaviour of the shape functions when applied to linear elliptic problems solved by iterative methods [9,12,34]. In this sense, the local analysis are useful for the appropriate selection of the p-basis in the context of iterative methods and algebraic multigrid [16].

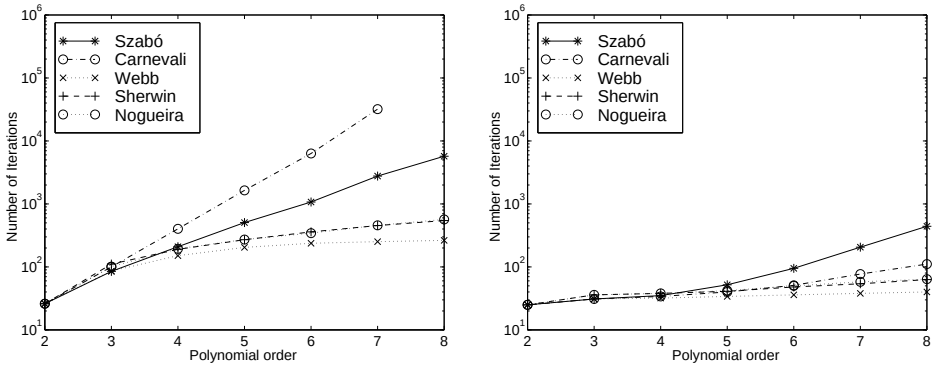

(a) Square domain.

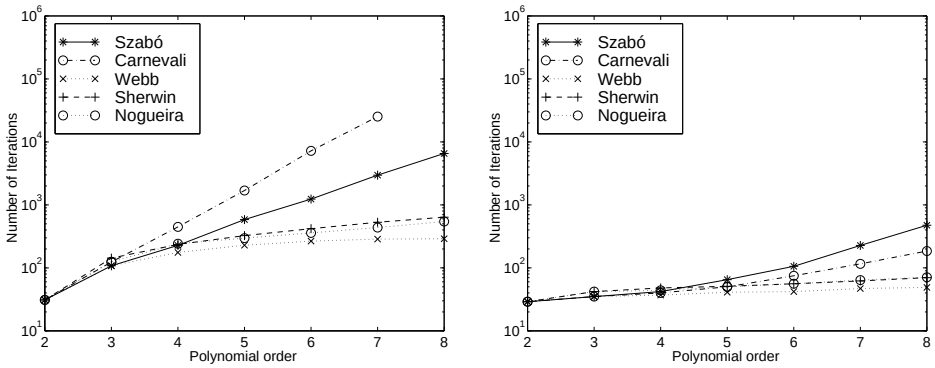

(b) L-shaped domain.

Figure 5: Number of iterations for the standard and Jacobi conjugate gradient methods versus the polynomial order for the square and L-shaped domains.

Based on the previous global results and the local analysis presented in [15], the shape functions developed in [1,32] have the lowest increasing rate of the condition number in terms of the polynomial order p. Although this set of basis functions has demonstrated an excellent performance from the conditioning point of view the functions presented by [15, 27] have also showed remarkable results with the advantage of using a tensorial formulation which optimizes numerical and computational efficiency. These arguments has led to the adoption of the Spectral/hp basis functions to approximate the solution of the considered linear and non-linear elastic structural problems.

4.2 Linear elasticity problems

This section presents results of the application of the Spectral/hp FEM to two linear and one non-linear elastic problems. The first problem has analytical solution and the energy norm of the error is calculated as the approximation space is refined. The other two examples do not have analytical solution and the error energy norm is estimated based on the *a posteriori*-estimate given in [28]. The results are also compared with those ones obtained using the ANSYS commercial software.

4.2.1 Cantilever beam

Figure 6 shows the finite element mesh of tetrahedra used for the vertical prismatic cantilever beam with quadrangular cross-section subjected to its own weight. The global coordinate system and the boundary conditions on the superior face of the beam are indicated. The cross section dimensions are $l = 1.0\,m$ and $h = 1.0\,m$. Three beam lengths are considered, i.e., $c = 3.0\,m$, $9.0\,m$ and $18.0\,m$. The material properties are density ($\rho = 7885.0\,kg/m^3$), Young's modulus ($E = 210.0\times10^9\,N/m^2$) and Poisson's ratio ($\nu = 0,3$). The gravity acceleration is $g = 9.81\,m/s^2$. The finite element meshes have 18 tetrahedral along the length of the beam (y axis).

The boundary conditions on the superior face of the beam were applied as follow: one vertex has all the three displacement components zero; another vertex has only the y and z component with zero displacements; the other two vertices have zero displacements in the y-direction. The way boundary conditions were applied follows [13]. The analytical solution of this problem, $\mathbf{u}_{ex} = (u_x, u_y, u_z)$, is [30]

$$\begin{aligned} u_x &= \frac{\nu\rho g}{2E}(2xy - 2cx - y), \\ u_y &= \frac{\rho g}{2E}\{2cy - y^2 - \nu(x^2 + z^2 - x - z)\}, \\ u_z &= \frac{\nu\rho g}{2E}(2yz - 2cz - y). \end{aligned} \tag{40}$$

The respective strain and stress components are given by

$$\begin{aligned} \gamma_{xy} &= \gamma_{xz} = \gamma_{yz} = 0, \varepsilon_{xx} = \varepsilon_{zz} = -\frac{\nu\rho g}{E}(c - y), \varepsilon_{yy} = \frac{\rho g}{E}(c - y), \\ \sigma_{xx} &= \sigma_{zz} = \tau_{xy} = \tau_{xz} = \tau_{yz} = 0, \sigma_{yy} = \rho g(c - y). \end{aligned} \tag{41}$$

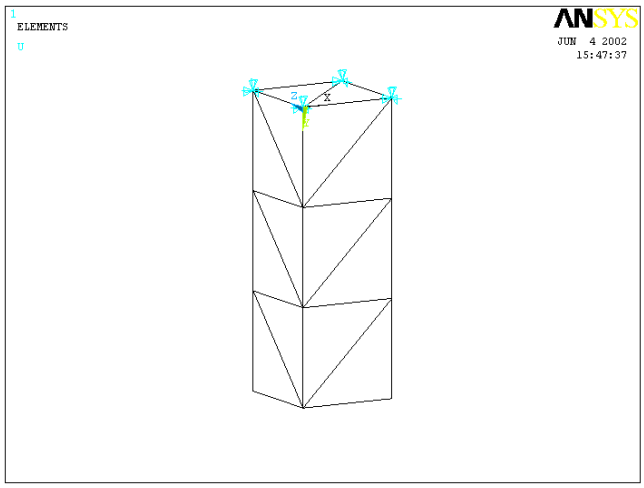

Figure 6: Mesh of tetrahedral for the prismatic cantilever beam.

From the previous expressions, the energy norm of the exact solution may be calculated, where it should be observed that only σ_{yy} contributes to the strain energy. Therefore,

$$\|\mathbf{u}_{ex}\|^2_{E(\Omega)} = \frac{1}{2}\mathcal{B}(\mathbf{u}_{ex}, \mathbf{u}_{ex}) = \frac{1}{2}\int_\Omega \sigma_{yy}\varepsilon_{yy} dV. \tag{42}$$

The substitution of the expressions for σ_{yy} and ε_{yy} given in (41) results in

$$\int_\Omega \sigma_{yy}\varepsilon_{yy} dV = \frac{(\rho g)^2}{E}\int_0^h \int_0^l \int_0^c (c-y)^2 dx dy dz. \tag{43}$$

Using the given values for the material properties and dimensions results in the following values for the energy norm of the exact solution for each of the three lengths and 8-digit accuracy

$$\begin{aligned} \|\mathbf{u}_{ex}\|^2_{E(\Omega)} &\approx 0.12821376 \quad (c = 3.0\,m), \\ \|\mathbf{u}_{ex}\|^2_{E(\Omega)} &\approx 3.46177146 \quad (c = 9.0\,m), \\ \|\mathbf{u}_{ex}\|^2_{E(\Omega)} &\approx 27.69417169 \quad (c = 18.0\,m). \end{aligned} \tag{44}$$

The energy norm of the error in the Galerkin-FEM approximated solution is [28]

$$\|\mathbf{e}\|^2_{E(\Omega)} = \|\mathbf{u}_{ex}\|^2_{E(\Omega)} - \|\mathbf{u}\|^2_{E(\Omega)}\,. \tag{45}$$

The energy norm of the approximated solution $\{\mathbf{u}\}$ is obtained straightforward using (32),

i.e.,

$$\|\mathbf{u}\|_{E(\Omega)} = \sqrt{\frac{1}{2}\mathcal{B}_p(\{\mathbf{u}\},\{\mathbf{u}\})}, \tag{46}$$

$$\mathcal{B}_p(\{\mathbf{u}\},\{\mathbf{u}\}) = \{\hat{\mathbf{u}}\}^T\left[\int_\Omega([B]^T[C][B])dV\right]\{\hat{\mathbf{u}}\} = \{\hat{\mathbf{u}}\}^T[\mathbf{K}]\{\hat{\mathbf{u}}\} = \{\hat{\mathbf{u}}\}^T\{\mathbf{f}\}. \tag{47}$$

Figures 7(a) and 7(b) show the relative error in the energy norm for the three lengths of the beam in terms of the number of degrees of freedom N related to the polynomial orders $p = 1, \ldots, 8$ and the square root of N, respectively, as plotted in [28].

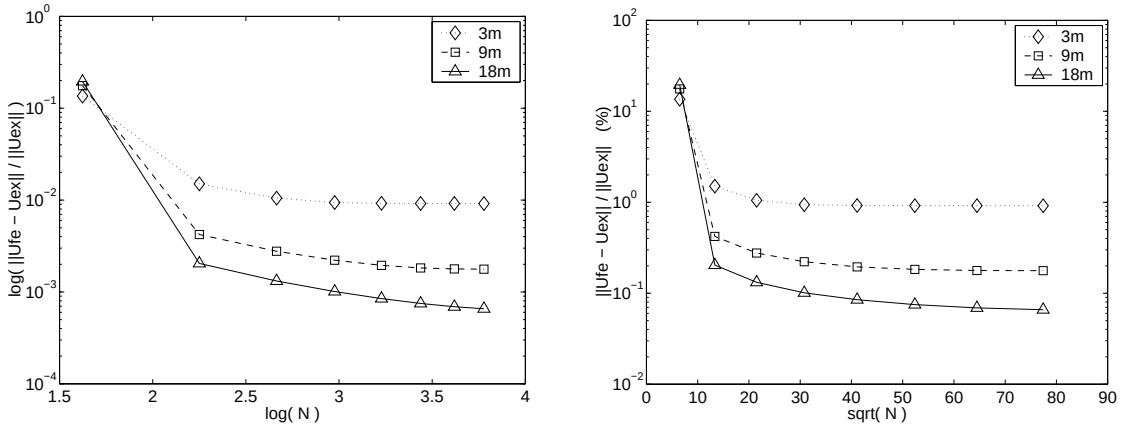

(a) Relative error × number of degrees of freedom. (b) Relative error × $\sqrt{}$number of degrees of freedom.

Figure 7: Relative error for the approximated solutions of the cantilever beam in terms of the number of degrees of freedom for $p = 1, \ldots, 8$ and the three lengths of the beam.

It should be observed that the error in the energy norm is not zero for $p \geq 2$ as it would be expected. This behaviour may be explained due to the way boundary conditions affect the global mesure of the error in energy norm. Local perturbations in the approximated solution may occur due to the Saint-Venant's Principle [30]). As the beam length is increased, the error decreases. The previous hypotheses may be verified in Figure 8 which shows the error of the vertical displacement of node $(x, y, z) = (1, c, 1)$ located on the free end of the beam in terms of the polynomial order. The quadratic feature of the exact and approximated solutions may be observed.

4.2.2 Cantilever beam with body and surface loads

In this example, a cantilever beam is subjected to its own weight and a surface load. The finite element solutions is obtained for $p = 1, ..., 8$ for three meshes with 34, 65 and 102 tetrahedral as illustrated in Figure 9. The boundary conditions and the constant $10^4\, N/m^2$ surface load

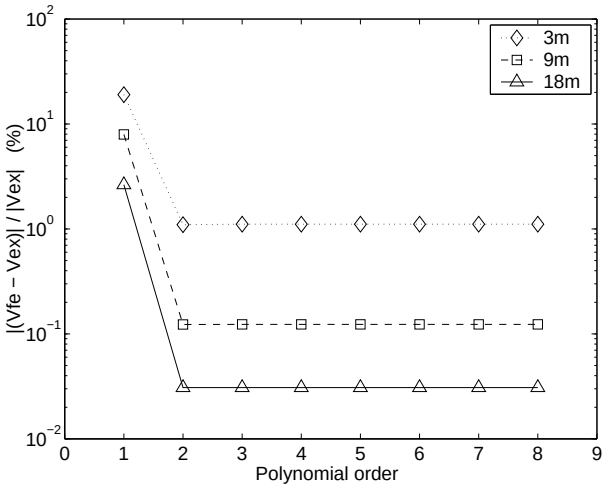

Figure 8: Percentual error of the vertical displacement u_y of node $(x, y, z) = (1, c, 1)$ versus the polynomial order.

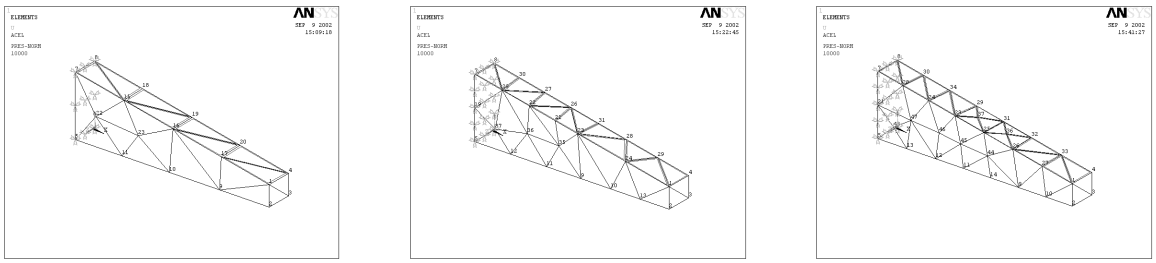

(a) 34 elements. (b) 65 elements. (c) 102 elements.

Figure 9: Meshes used in the second example.

applied on the negative direction of the superior face are also illustrated. The dimensions of the beam are $c = 2.0\,m, l_1 = 0.6\,m, l_2 = 0.2\,m, h = 0.2\,m$. The material properties are the same ones used in the previous example.

As the considered problem does not have an analytical solution, the approximation error in the finite element solutions will be calculated using the *a-posteriori* error estimate in the energy norm given in [28]. This estimate uses the energy of the solution for three refinement levels $p, p-1$ and $p-2$. Based on these values and the number of degrees of freedom for each level, it is possible to estimate the energy of the exact solution.

From equation (45) and the *a-priori* error estimate indicated in [5], the energy norm of the error in the finite element approximation may be expressed as

$$\|\mathbf{e}\|^2_{E(\Omega)} = \|\mathbf{u}_{ex} - \mathbf{u}\|^2_{E(\Omega)} = \Pi(\mathbf{u}_{ex}) - \Pi(\mathbf{u}) \approx \frac{k^2}{N^{2\beta}}, \tag{48}$$

where k and β are positive constants (β is related to the regularity of the exact solution), N is the number of degrees of freedom and $\Pi(\cdot)$ the energy of the solution. There are 3 unknowns in the previous equation $\Pi(\mathbf{u}_{ex}), k$ and β. Taking the finite element solutions for three values of p, the unknowns may be calculated and the following relation is obtained [28]

$$\frac{\log \dfrac{\Pi - \Pi_p}{\Pi - \Pi_{p-1}}}{\log \dfrac{\Pi - \Pi_{p-1}}{\Pi - \Pi_{p-2}}} \approx \frac{\log \dfrac{N_{p-1}}{N_p}}{\log \dfrac{N_{p-2}}{N_{p-1}}}, \tag{49}$$

where Π is the energy of the exact solution; $\Pi_p, \Pi_{p-1}, \Pi_{p-2}$ and N_p, N_{p-1}, N_{p-2} are the energy of the finite element solutions and the numbers of degrees of freedom for the approximation spaces $p, p-1$ and $p-2$, respectively. Denoting the right hand side of the previous equation by Q, it follows that

$$\frac{\Pi - \Pi_p}{\Pi - \Pi_{p-1}} \approx \left(\frac{\Pi - \Pi_{p-1}}{\Pi - \Pi_{p-2}} \right)^Q. \tag{50}$$

The previous *a-posteriori* estimate assumes monotonic convergence of Π_p and implies the nestedness of the approximation spaces for different polynomial orders, i.e., $S^{p-2} \subset S^{p-1} \subset S^p$, which is valid for the p-version due to the hierarchy of the spaces.

Figures 10 shows the convergence behaviour of the approximated solution obtained using the h and p-versions of the FEM for each of three meshes used. The convergence is compared based on the error in the energy norm versus the number of degrees of freedom in the log-log scale. The p-refinements were obtained for $p = 1, \ldots, 8$. The h-refinements are represented by the dashed lines which were extrapolated based on the solutions for the meshes of 34, 65 and 102 linear tetrahedral. The legend of each plot indicates the angular coefficients of the fitted lines for the h and p-versions. The calculation of the p-coefficients do not take in account the pre-asymptotic behaviour between $p = 1$ and $p = 2$.

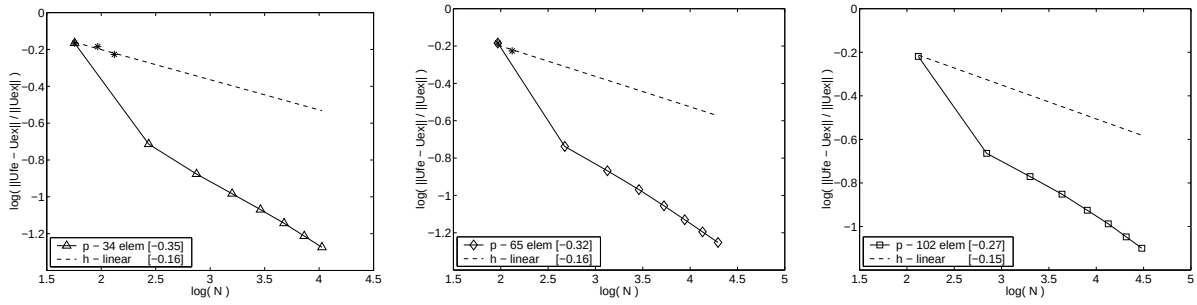

(a) 34 elements. (b) 65 elements. (c) 102 elements.

Figure 10: Relative error in the energy norm versus the number of degrees of freedom for the second example.

Based on these results, it may be observed that the error coefficient for the p-version is about twice the error for the h-refinement. This behaviour agrees with the theoretical estimates of exponential convergence rate for p-refinements [28].

The estimates of the exact solution energy with 8-digit accuracy for the three meshes are, respectively,

$$\begin{aligned} \Pi(u) &\approx 0.08464549 \quad \text{(34 elements)}, \\ \Pi(u) &\approx 0.08483894 \quad \text{(65 elements)}, \\ \Pi(u) &\approx 0.08634225 \quad \text{(102 elements)}. \end{aligned} \tag{51}$$

Figure 11 shows the behaviour of the relative error of the approximated solutions obtained using the p-version for $p = 1, \ldots, 8$ in terms of the square root of the number of degrees of freedom for each one of the three meshes used.

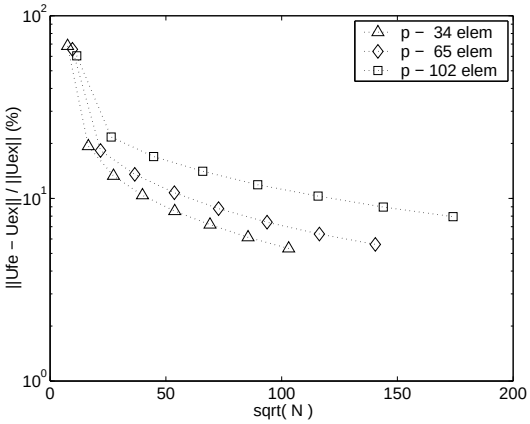

Figure 11: Percentual relative error versus the number of degrees of freedom for three meshes of the second example.

It should be observed the interesting behaviour of the decrease of the accuracy with the increasing of the number of elements. The error estimate in the energy norm used are entirely based on p-refinements and it seems not adequate for the hp-version. It may also be observed the low accuracy of the linear solutions which may be explained due to the greater stiffness of the linear tetrahedra when used in the approximation of the elasticity operator.

Table 1 compares the displacement components for one node of the 3 meshes based on the solutions obtained from the ANSYS program and the Spectral/hp FEM used in this paper. ANSYS implements a p-error estimator with a non-uniform refinement of the elements. The refinement stopping criterion is based on the difference of the strain energies of each element between two successive refinements and the user-supplied accuracy, which was 1% for the considered example. The polynomial order indicated in Table 1 for the ANSYS solutions are related to the most predominant order found in the elements of the meshes, which is in general the largest

order. The results for the two formulations have a reasonable correlation for the nodal solutions. As it would be expected, the u_z displacement components tend to zero and the values obtained from ANSYS oscillates around zero. The Spectral/*hp* u_z values are greater than the respective ANSYS absolute values. This behaviour may be explained due to the singularity of the local transformations applied to the definition of the shape functions. Anyway, the convergence of the FEM is based on the energy norm of error and not locally in each point of the domain. The contribution of the u_z displacement in the energy norm is minimal for both solutions.

Table 1: Comparison of nodal solution obtained using the ANSYS software and the Spectral/*hp* FEM for the second example.

			Displacement $\mathbf{u}$ $[m]$		
Mesh	Node	Formulation	u_x	u_y	u_z
34 elem.	1	ANSYS	0,54665e-05	-0,32492e-04	-0,29401e-08
$p = 4$		Spectral/*hp*	0,54970e-05	-0,32792e-04	0,60912e-06
65 elem.	1	ANSYS	0,54679e-05	-0,32501e-04	-0,80350e-08
$p = 4$		Spectral/*hp*	0,55637e-05	-0,32834e-04	0,10157e-06
102 elem.	1	ANSYS	0,54621e-05	-0,32470e-04	0,14558e-09
$p = 3$		Spectral/*hp*	0,54983e-05	-0,32734e-04	0,31620e-06

4.3 Non-linear elasticity

The Spectral/*hp* FEM considered in this paper will be applied to the problem of large deformation of a cantilever beam submitted to its own weight and a constant surface load. The mesh used of 23 tetrahedra, the boundary conditions and surface load are illustrated in Figure 12. The dimensions of the beam are $c = 3.0\,m \times l = 0.3\,m \times h = 0.05\,m$. The material properties are $\rho = 250.0\ kg/m^3$, $E = 4.0 \times 10^8\ N/m^2$ and $\nu = 0.3$. The surface load intensity is $100.0\,N/m^2$ and applied in the negative y-direction. The solutions were obtained for $p = 1, \ldots, 8$ using the Newton-Raphson method with one load step. The energy stop criterion in the Euclidian norm were used with 10^{-4} precision. The results are compared for one node of the mesh with the non-linear formulation of the ANSYS software based on the h-version and taking the equivalent numbers of degrees of freedom for the two formulations.

Figures 13(a) and 13(b) show the convergence behaviour of the solutions in the non-linear cantilever beam when the approximation space is refined for $p = 1, \ldots, 8$. The convergence is indicated, respectively, in terms of the logarithmic and percentual of the relative error in the energy norm versus the number of degrees of freedom. Figure 13(a) also shows the comparison of the relative errors for the h and p versions of FEM. The results for the h-version were extrapolated based on the solutions calculated for meshes of 23, 33, 64 and 108 elements.

As in the linear case, it may be observed from Figure 13(a) that the p-version has an exponential convergence rate for the non-linear cantilever beam. The rate of convergence of the p-version is very superior when compared with the results obtained for h-version. For non-linear

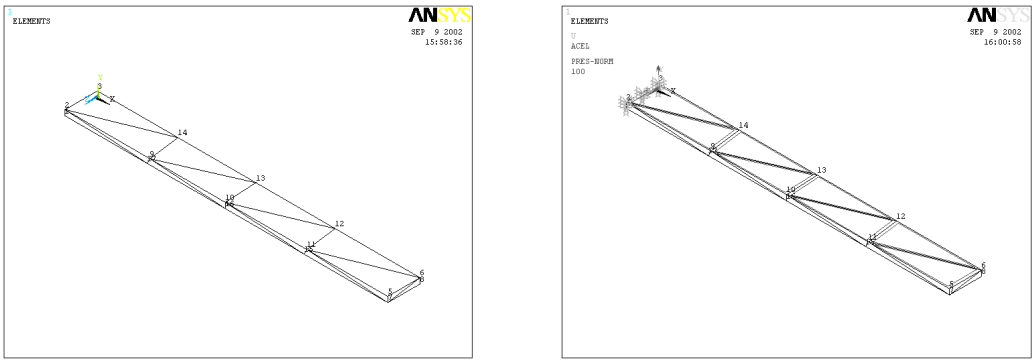

(a) Mesh with 23 elements. (b) Boundary conditions.

Figure 12: Non-linear cantilever beam.

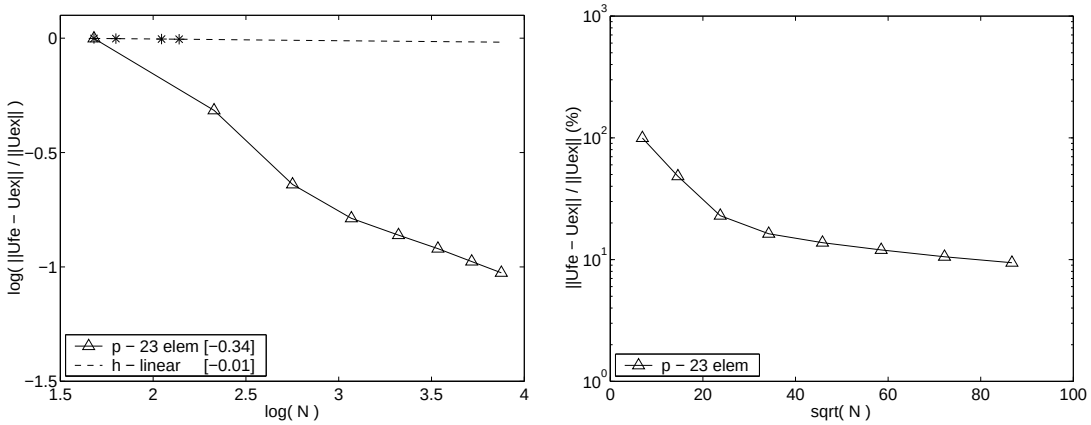

(a) Relative error vs. number of dofs. (b) Percentual relative error vs. $\sqrt{}$number of dofs.

Figure 13: Error behaviour for the non-linear cantilever beam.

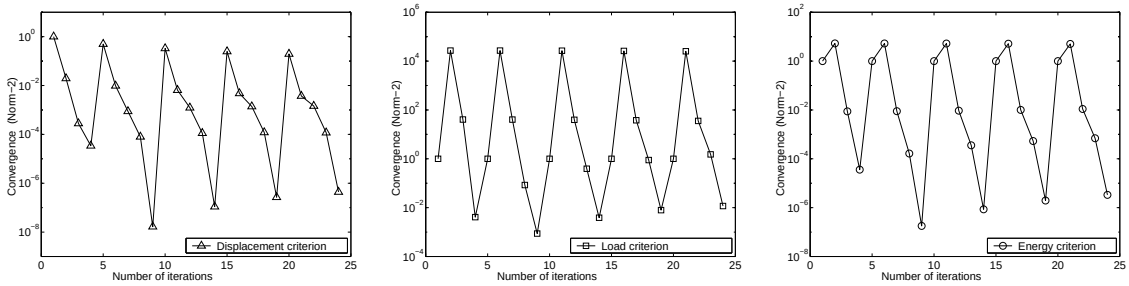

(a) Displacement criterion. (b) Load criterion. (c) Energy criterion.

Figure 14: Convergence of Newton-Rhapson iterations for the three convergence criteria versus the total number of iterations and $p = 5$.

problems, the larger stiffness produced by the linear Lagrange elements is more critical when compared to the linear case.

The estimate of the energy of the exact solution for the mesh with 23 elements using the *a-posteriori* estimate given [28] is

$$\Pi(u) \approx 21.19735351. \tag{52}$$

For the mesh with 23 elements illustrated in Figure 12(a) and polynomial order $p = 5$, Figure 14 shows the behaviour of the non-linear solution obtained with 5 load steps according to the Euclidian norm of the load, displacement and energy criteria of the Newton-Rhapson procedure [8]. It may be observed that the convergence criteria are not absolutely equivalent in terms of the norms of their respective expressions used to measure convergence. The energy criterion has an intermediate behaviour and is situated between the limits of the displacement and load criteria.

For the same conditions used in the previous test of the convergence criteria, Figure 15 shows the displacements in the y-direction for one node of the mesh obtained from the linear and non-linear models. Due to the non-linear stiffness, the displacement at the end of each load step is lower than that of the linear case.

Table 2 presents the comparison of the displacement components for one node of the mesh calculated using the ANSYS program and the Spectral/*hp* FEM. Two different meshes were used. The p-mesh has 23 tetrahedral and polynomial order $p = 5$. The ANSYS mesh has 303 quadratic tetrahedral. For both meshes, the number of degrees of freedom is 2100. The displacement and load convergence criteria were used simultaneously in the ANSYS program. The precisions were 10^{-3} and 10^{-6} for the load and displacement convergence criteria, respectively. For the Spectral/*hp* FEM, the energy criterion was used with 10^{-4} precision. The results have a reasonable agreement which shows that the Spectral/*hp* Methods are suitable also for non-linear solid mechanic problems.

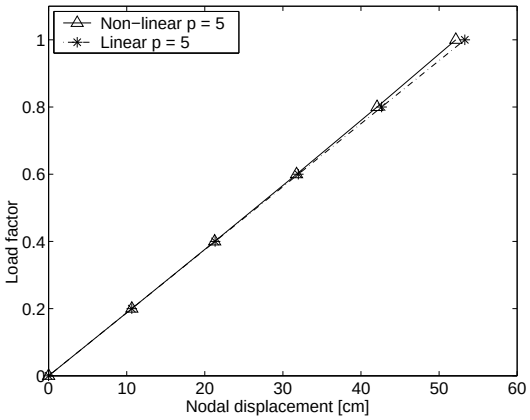

Figure 15: Load steps versus the nodal y-displacement for the linear and non-linear models.

Table 2: Comparison of the nodal solution for the non-linear cantilever beam obtained from the ANSYS program and the Spectral/*hp* Method.

				Displacement $\mathbf{u}$ $[m]$		
Mesh	DOFs	Node	Formulation	u_x	u_y	u_z
h	2100	5	ANSYS	-0,46644e-01	-0,52177	0,50587e-04
$p = 5$	2100	5	Spectral/*hp*	-0,46630e-01	-0,52143	-0,13399e-03

5 Conclusions

Based on the results obtained in this paper, it is possible to conclude that the Spectral/*hp* FEM proposed in [17] for CFD problems in 3D non-structured meshes are also applicable to linear and non-linear elasticity problems. From the local side, this method has the advantages of using high-order tensorial integration quadratures and high-order local numerical differentiation. For the global viewpoint, the construction of C^0 approximations may be obtained in a consistent and direct way in a pre-processing step. For linear and non-linear elasticity problems considered in this paper, it should be advisable to use a quadratic element to start the p-refinement procedure due to the poor stiffness representation of the linear elements.

References

[1] R. Abouchakra. Hierarchal tetrahedral elements using orthogonal polynomials. In *1996 Canadian Conference on Electrical and Computer Engineering (CCECE'96)*, volume 18, pages 525–528, Calgary, 1996. part 2 (of 2).

[2] S. Adjerid, M. Aiffa, and J.E. Flaherty. Hierarchical finite element bases for triangular and tetrahedral elements. *Comput. Methods Appl. Mech. Engrg.*, 190:2925–2941, 2001.

[3] O. Axelsson and V.A. Barker. *Finite element solution of boundary value problems – theory and computation*. Academic Press, Orlando, 1984.

[4] I. Babuška, M. Griebel, and J. Pitkaranta. The problem of selecting the shape functions for p-type finite elements. *Int. J. Numer. Methods Engrg.*, 28:1891–1908, 1989.

[5] I. Babuška, B. A. Szabó, and I. N. Katz. The p-version of the finite element method. *SIAM J. Numer. Anal.*, 18(3):515–545, 1981.

[6] M.L. Bittencourt. Fully tensorial nodal and modal shape functions for triangles and tetrahedra. *Int. Journal for Numerical Methods in Engineering*, 63:1530–1558, 2005.

[7] M.L. Bittencourt. Construction of shape functions for the h- and p-versions of the fem using tensorial product. *Int. Journal for Numerical Methods in Engineering*, 2006. in press.

[8] J. Bonet and J. Peraire. An alternating digital tree (ADT) algorithim for 3D geometric searching. *International Journal for Numerical Methods in Engineering*, 38:3529–3544, 1995.

[9] P. Carnevali, R. B. Morris, Y. Tsuji, and G. Taylor. New basis functions and computational procedures for p-version finite element analysis. *Int. J. Numer. Methods Engrg.*, 36:3759–3779, 1993.

[10] P.B.R. Devloo, J.T. Oden, and P. Pattani. Shape optimization of structures: A literature survey. *Comput. Meth. Appl. Mech. Engrg.*, 70:203–235, 1988.

[11] D. A. Dunavant. High degree efficient symmetrical gaussian quadrature rules for the triangle. *Int. J. Numer. Methods Engrg.*, 21:1129–1148, 1985.

[12] N. B. Edgar and K. S. Surana. On the conditioning number and the selection criteria for p-version approximation functions. *Computers and Structures*, 60(4):521–530, 1996.

[13] N. Hu, X.-Z. Guo, and I. N. Katz. Multi-p preconditioners. *SIAM J. Sci. Comput.*, 18(6):1676–1697, 1997.

[14] A.C. Nogueira Jr. *Formulação p do Método de Elementos Finitos em Problemas de Elasticidade Linear e Não-Linear com Malhas 3D Não-Estruturadas e em Métodos Multigrid Algébricos*. PhD thesis, Faculdade de Engenharia Mecânica, Universidade Estadual de Campinas, 2002.

[15] A.C. Nogueira Jr. and M.L. Bittencourt. Hierarchical basis functions for the p-version of the finite element method (in portuguese). *Revista Internacional de Métodos Numéricos para Cálculo y Diseño en Ingeniería*, 17(1):37–59, 2001.

[16] A.C. Nogueira Jr. and M.L. Bittencourt. Algebraic multigrid schemes for the p-version of the finite element method applied to 3D elliptical problems. In *Proceedings of the 5th World Congress on Computational Mechanics (WCCM V)*, Vienna - Austria, 2002. Technical University of Vienna and IACM.

[17] G. E. Karniadakis and S. J. Sherwin. *Spectral/hp Element Methods for CFD*. Oxford University Press, Oxford, 1999.

[18] I.N. Katz. Nodal variables for complete conforming finite elements of arbitrary polynomial order. *Computers and Mathematics with Applications*, 4:85–112, 1978.

[19] W.M. Lai, D. Rubin, and E. Krempl. *Introduction to Continuum Mechanics*. Butterworth-Heinemann, 3rd edition, 1993.

[20] J.F. Maitre and O. Pourquier. About the conditioning of matrices in the p-version of the finite element method for second order elliptic problems. *Journal of Computational and Applied Mathematics*, 63:341–348, 1995.

[21] J. Mandel. Hierarchical preconditioning and partial orthogonalization for the p-version finite element method. In T. Chan, R. Glowinski, and O. Windlund, editors, *Proceedings of the 3th International Symposium on Domain Decomposition Methods for Partial Differential Equations*, pages 141–156, Huston, Texas, 1990. SIAM.

[22] J. Mandel. Two-level domain decomposition preconditioning for the p-version finite element method in three dimensions. *Int. J. Numer. Methods Engrg.*, 29:1095–1108, 1990.

[23] A.A. Novotny, R.A. Feijóo, C. Padra, and E. Taroco. Gradiente topológico via análise de sensibilidade à mudança de forma na otimização topológica. Report, LNCC, Laboratório Nacional de Computação Científica, Rio de Janeiro, 2000.

[24] A.G. Peano. Hierarchies of conforming finite elements. Master's thesis, Washington University - St. Louis, 1975.

[25] A.G. Peano. Hierarchies of conforming finite elements for plane elasticity and plate bending. *Computers and Mathematics with Applications*, 2:211–224, 1976.

[26] M.P. Rossow and I.N. Katz. Hierarchical finite elements and precomputed arrays. *Int. J. Numer. Methods Eng.*, 12:977–999, 1993.

[27] S.J. Sherwin and G.E. Karniadakis. A new triangular and tetrahedral basis for high-order (hp) finite element methods. *Int. J. Numer. Methods Engrg.*, 38:3775–3802, 1995.

[28] B. A. Szabó and I. Babuška. *Finite Element Analysis*. Wiley Interscience, New York, 1991.

[29] B. A. Szabó and A. G. Peano. Hierarchic finite elements. In H. Kardestuncer and D.H. Norrie, editors, *Finite Element Handbook*, pages 2227–2233. McGraw-Hill, New York, 1987.

[30] S.P. Timoshenko and J.N. Goodier. *Theory of Elasticity*. McGraw-Hill, 3rd edition, 1970.

[31] S.M. Vijayakar, H.R. Busby, and D.R. Houser. Finite element analysis of quasi-prismatic bodies using Chebyshev polynomials. *Int. J. Num. Meth. Engrg.*, 24:1461–1477, 1987.

[32] J. P. Webb and R. Abouchakra. Hierarchal triangular elements using orthogonal polynomials. *Int. J. Numer. Methods Engrg.*, 38:245–257, 1995.

[33] O.C. Zienkiewicz, D.W. Kelly, J.P. de S.R. Gago, and I. Babuška. Hierarchical finite element approaches, error estimates and adaptive refinement. In *MAFELAP*, pages 313–346, Brunel University, 1981.

[34] G. Zumbusch. *Simultaneous h-p adaption in multilevel finite elements*. PhD thesis, Freien Universitat Berlin, Germany, 1995.